Contributed paper

OPTO-ELECTRONICS REVIEW **6**(3), 217–230 (1998)

# Investigation of InAsSb infrared photodetectors for near room temperature operation

J.D. KIM and M. RAZEGHI*

Center for Quantum Devices, Department of Electrical and Computer Engineering, Northwestern University, Evanston, IL 60208, USA

*Long-wavelength infrared (LWIR) photodetectors operating at near room temperature are highly desirable for a number of applications. Narrow bandgap semiconductors have been long researched for applications in the infrared photodetectors and much progress has been made on the II-VI compounds. Recent rapid development in epitaxial thin film growth techniques made it possible to explore the more promising III-V material systems. In this article, we report the recent results on the near room temperature operation of III-V $InAs_{1-x}Sb_x$ photodetectors. $InAs_{1-x}Sb_x$ detector structures were grown on GaAs substrates by low-pressure metalorganic chemical vapor deposition (LP-MOCVD). The structural, optical, and electrical properties of this material were investigated in detail. Device modeling has been performed prior to the growth of detector structures. Photoconductive detectors with $x = 0.77$ exhibited photoresponse up to 14 μm at 300 K. Corresponding effective lifetime of ~ 0.14 ns and Johnson noise limited detectivity at 10.6 μm of $3.3 \times 10^7$ cmHz$^{1/2}$/W have been obtained at 300 K. Because of many advantages of the photovoltaic devices, photovoltaic detectors have been also fabricated. A room-temperature photoresponse of up to 13 μm has been observed at 300 K with a $x \sim 0.85$ sample and $R_0A$ product of ~ $10^{-5}$ Ωcm$^2$. These results showed the feasibility of using $InAs_{1-x}Sb_x$ for uncooled photodetector applications as an alternative to $Hg_{1-x}Cd_xTe$.*

## 1. Introduction

Photodetectors operating in the 8–12 μm wavelength range are of great importance for applications in infrared thermal imaging because 8–12 μm infrared band is the most important atmospheric window in detecting room temperature objects. The energy density radiated from the objects at room temperatures is maximum and the atmospheric absorption is minimum in this window [1]. Therefore, LWIR detectors have found numerous military and civilian applications in night vision, reconnaissance, guidance, ranging, industrial thermography, medical imaging, meteorological research, and communication systems.

For this purpose, thermal detectors such as bolometers, pyroelectric detectors, and thermocouples can be operated at ambient temperature [2]. Uncooled thermal detectors are lightweight, rugged, reliable, and convenient to use. However, their detectivity is low, especially when operated at high frequencies. A high sensitivity and fast response detection of infrared radiation can be achieved with the use of semiconductor photodetectors [3]. One of the major drawbacks of infrared photodetectors is the need for cooling to suppress thermal processes that compete with the optical ones in the generation of free carriers in the semiconductor. The need for cooling is a considerable problem that inhibits the more wide spread use of infrared systems. The cooling requirements add considerably to the cost, bulk, weight, and power consumption, so it is highly desirable that they be eliminated. To overcome these problems originated from cryogenic cooling, there have been a lot of theoretical and experimental works to develop uncooled infrared photodetectors [4–8].

HgCdTe has been the most important intrinsic semiconductor material for both cooled and uncooled LWIR photodetector applications. HgCdTe can cover the entire infrared spectrum by varying Hg to Cd ratio within the crystal. Because of this advantage, HgCdTe has been one of the most thoroughly studied semiconductors outranked only by Si and GaAs [9].

* e-mail: razeghi@ece.nwu.edu

But at the same time, HgCdTe is one of the most difficult materials to use for infrared detectors because of the problems caused by lattice, surface, and interface instabilities. These problems originate from weak bonding characteristics of II-VI semiconductors and from high Hg vapor pressure. Weak bonding reduces the strength of the material, resulting in a bad mechanical property and creating difficulties in the material processing. Moreover high Hg vapor pressure makes the composition control over a large area difficult, causing serious problems for the focal plane arrays (FPAs) applications. This has intensified the search for alternative infrared material systems.

As alternative to the current market dominant HgCdTe, a number of III-V semiconductor systems such as InAsSb [10–13], InSbBi [14–21], and InTlSb [22–24] have been studied because they offer promising material properties and highly advanced III-V material processing technologies. Among these material systems, InAsSb system is well developed and offers the lowest bandgap so far.

Earlier data suggested that InAsSb can exhibit a cutoff wavelength of only up to 10 μm at 77 K and 12.5 μm at 300 K. However, recent experimental results have demonstrated that the cutoff wavelength of InAsSb material can be extended to longer than 12.5 μm at 300 K [11]. Moreover, theoretical work on the InAsSb photodetectors especially for near room temperature operation has been done by Rogalski et al. [25,26]. The results show the promise for LWIR InAsSb photodetectors operating at near room temperature. However, InAsSb photodetectors have poor performance at high temperatures due to strong thermal generation and recombination of the charge carriers. Several solutions have been proposed to suppress the noise due to Auger recombination [3,8]. These include the optimization of the detector structure by controlling the composition, doping level, and thickness.

To realize the room temperature operation of InAsSb photodetectors, the material parameters of the active layer have been optimized through calculation of the $R_0A$ product. Finite difference method has been applied to obtain the detailed carrier concentration, electric field, potential, and current density profiles of the device. Successful growth of high quality InAsSb layers and composition and doping level control have been achieved with LP-MOCVD technique. The fabricated InAsSb photodetectors operated at room temperature in the 8–13 μm range. These demonstrations show the feasibility of InAsSb material system for future uncooled infrared photodetector applications.

## 2. Device modeling

Prior to the growth of InAsSb photodetector structures, device analysis has been performed in both analytical and numerical way. These analyses are particularly important for the design of photovoltaic detectors. Analytical model has been used to obtain theoretical predictions of $R_0A$ product. The $R_0A$ product is controlled by diffusion limited mechanism and the dominant recombination mechanism was found to be Auger process. For better understanding of the device behavior, a numerical analysis has been performed by solving the carrier transport equations and Poisson's equation with finite difference method. The model calculates the profile of carrier concentrations, potential, electric field, generation-recombination rates, and current density. Carrier extraction and reduced generation-recombination rates have been observed for reverse biased p-π-n devices.

### 2.1. Analytical model analysis

To achieve the highest possible detectivity, the ratio of the optical carrier generation to the thermal carrier generation should be minimized. Also the volume of the region of non-zero photoelectric gain where the thermal generation and recombination occurs should be minimized. The optimization of the photovoltaic detector structure for a given material can be made by a proper selection of doping level and layer thickness. The detectivity of a thermal noise limited photodetector is given by

$$D^* = \frac{\lambda \eta q}{hc} \frac{(R_o A)^{1/2}}{(4kT)^{1/2}} \tag{1}$$

The $R_0A$ product is the main factor that reflects the quality of the p-n junction and is dependent on the doping level of the p-n junction. The optimization of proper doping type and level has been obtained through the calculation of $R_0A$ products for different doping types and levels. To calculate the $R_0A$ product, four dark current components from the bulk and depletion region were considered. They consisted of diffusion current due to Auger processes, diffusion current from radiative processes, generation-recombination (GR) current, and tunneling current.

In figure 1, $R_0A$ products from each process have been plotted as a function of temperature. The doping levels used for this simulation are $2 \times 10^{18}$ cm$^{-3}$ for the heavily doped region and $2 \times 10^{16}$ cm$^{-3}$ for the lightly doped region. It was clearly seen that the $R_0A$ product of the p-n junction was limited by generation

 © 1998 COSiW SEP, Warsaw

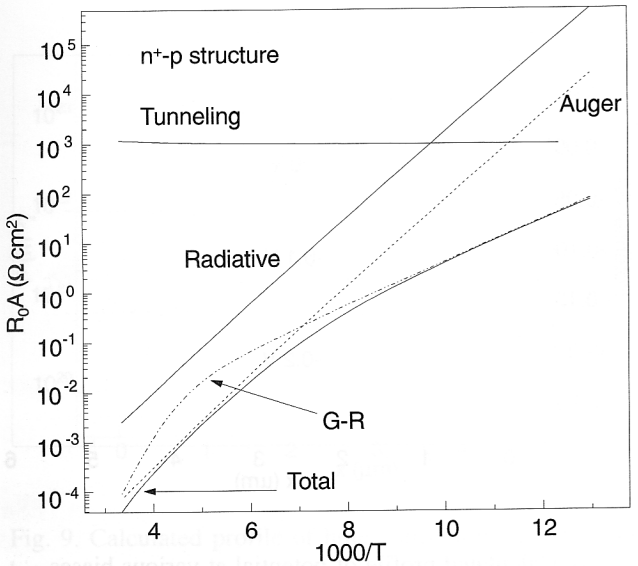


Fig. 1. Temperature dependence of the $R_0A$ product of an $InAs_{0.15}Sb_{0.85}$ p–n junction limited by various mechanisms.

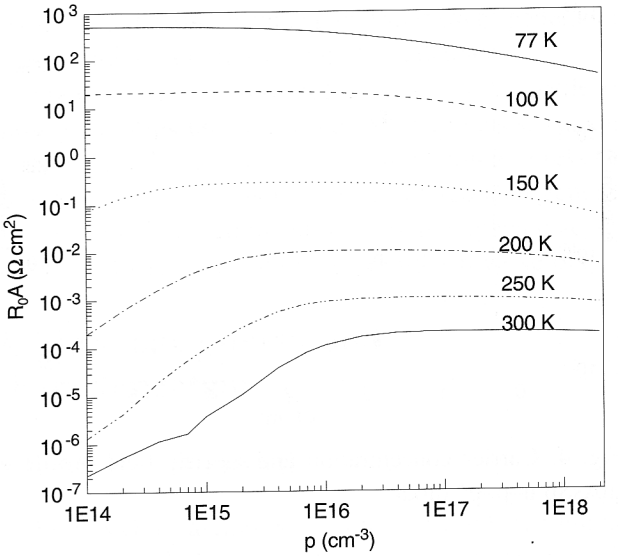


Fig. 3. P–doping level dependence of the $R_0A$ product of an $InAs_{0.15}Sb_{0.85}$ $n^+$–p junction at various temperatures.

recombination current at low temperatures and by Auger recombination at high temperatures

Same limiting processes have been found for the $p^+$-n structures. The total values of $R_0A$ for $n^+$-p and $p^+$-n diodes are plotted in Fig. 2 to see the doping type dependence of the $R_0A$ product. It is evident from the plot that the $n^+$-p junction exhibits a higher $R_0A$ value at room temperature than the $p^+$-n junction. These results indicate that the p-type active region ensures better performance for high temperature operation.

Once the doping type was determined, the doping level dependence of $R_0A$ was examined. $R_0A$ values at different temperatures and different doping levels have been calculated.

Figure 3 shows the doping level dependence of the $InAs_{0.15}Sb_{0.85}$ $n^+$-p photodiodes at different temperatures. Assuming 220 K operation using thermoelectric cooling, the optimum doping level has been determined to be around $3 \times 10^{16}$ $cm^{-3}$.

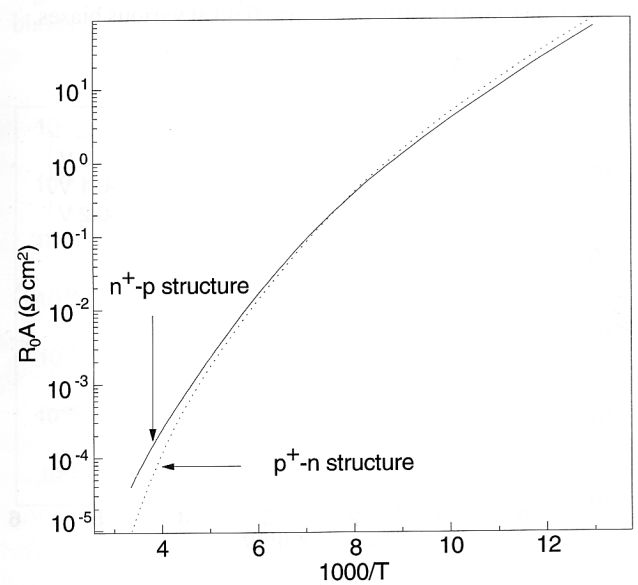


Fig. 2. Calculation of $R_0A$ for different types of InAsSb p–n junctions.

## 2.2. Numerical analysis

For simulation of more detailed device behavior at 300 K, numerical analysis of the photodiodes has been performed. The analysis has been done by solving the fundamental equations governing the electrical behavior of the InAsSb photodiode. Those equations consist of two current equations for electrons and holes, two continuity equations for electrons and holes, and Poisson's equation and they are collectively referred to as the Van Roosbroeck's equations. In order to execute a numerical analysis, the equations were transformed into the form of difference equations in which the variables were defined at a finite number of division points. The mesh point spacing was defined as a function of space coordinate x so that the fine spacing was chosen for the high field region and rough spacing was chosen for the low field region. The difference equations were then solved utilizing the Newton's iteration principle. More exact description of calculation methods can be found in Kurata's monograph [27] and Rogalski's paper [26]. Among the various G-R mechanisms, Auger 1 and Auger 7 processes are the most dominant processes at

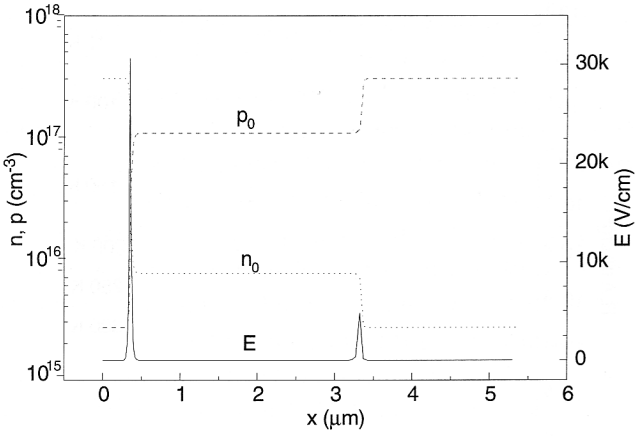


Fig. 4. Carrier concentration and electric field profile of InAsSb n–p–$p^+$ diode.

300 K. So only those mechanisms were considered for the estimation of G-R rates.

The device structure used for simulation was $p^+$-p-$n^+$ InAsSb diode. The profile of carrier concentration, potential, electric field, and current density across the devices has been calculated.

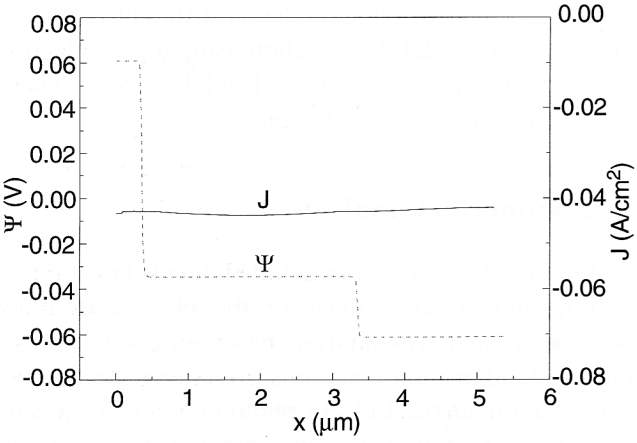


Fig. 5. Potential and current density profile of InAsSb n–p–$p^+$ diode.

Figures 4 and 5 show the profile plot of those quantities without any applied bias. To investigate the advantage of using $p^+$ top layer, comparison of p-$n^+$ and $p^+$-p-$n^+$ structures has been done. We were able to show that the dark current was lower by a factor of 3 and $R_0$ was higher by factor of 1.2 for $p^+$-p-$n^+$ structure. This shows the advantage of using $p^+$-p-$n^+$ structure instead of simple p-$n^+$ structure.

Further analysis has been done for the device behavior under reverse bias. The biasing has been incorporated through the change of the initial conditions of the potential. And the Van Roosebroeck's equation has been solved again with the new boundary conditions.

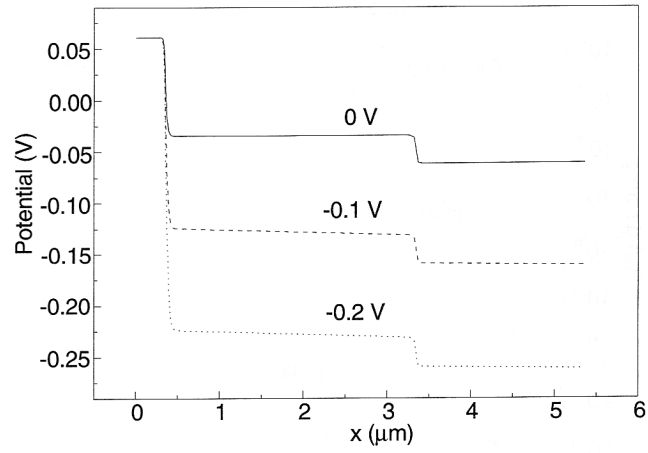


Fig. 6. Calculated profile of potential at various biases.

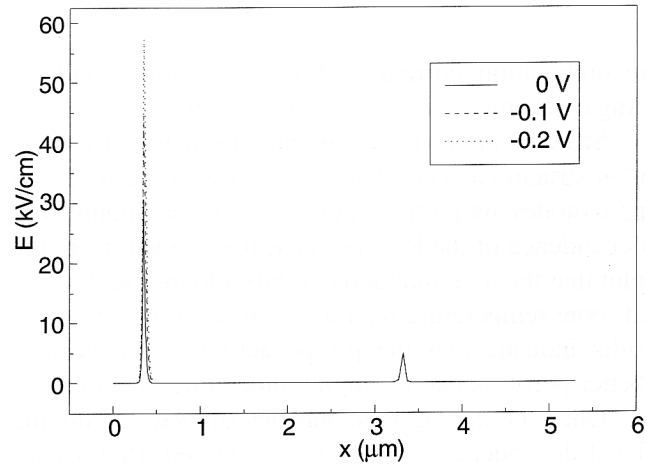


Fig. 7. Calculated profile of electric field at various biases.

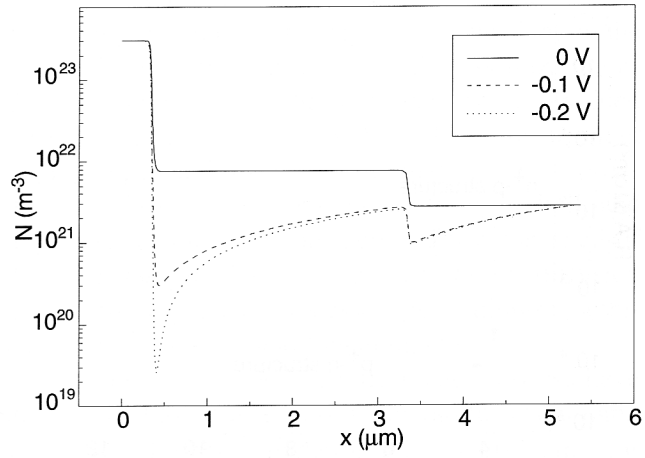


Fig. 8. Calculated profile of electron concentration at various biases.

 © 1998 COSiW SEP, Warsaw

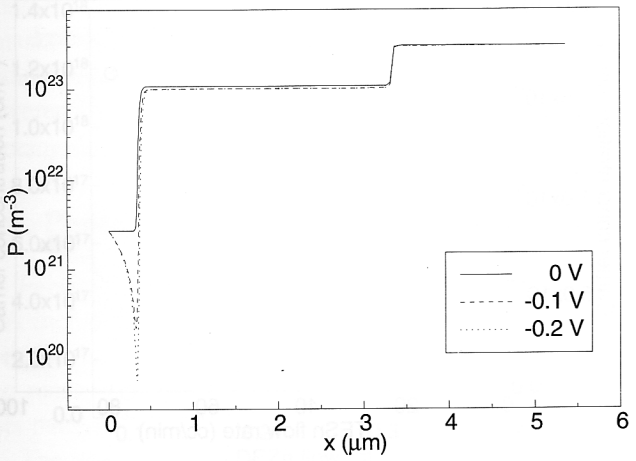


Fig. 9. Calculated profile of hole concentration at various biases.

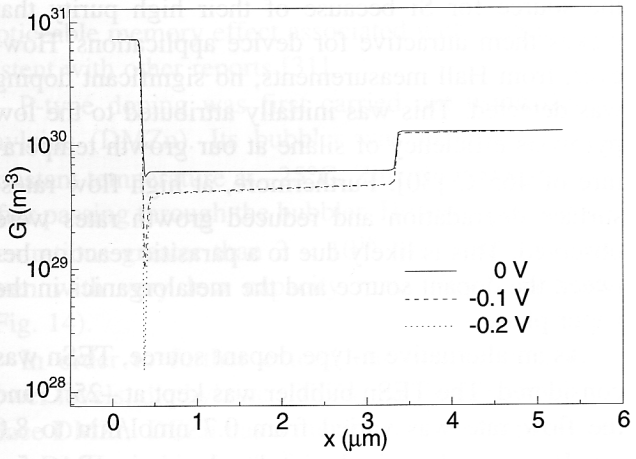


Fig. 10. Calculated profile of generation rate at various biases.

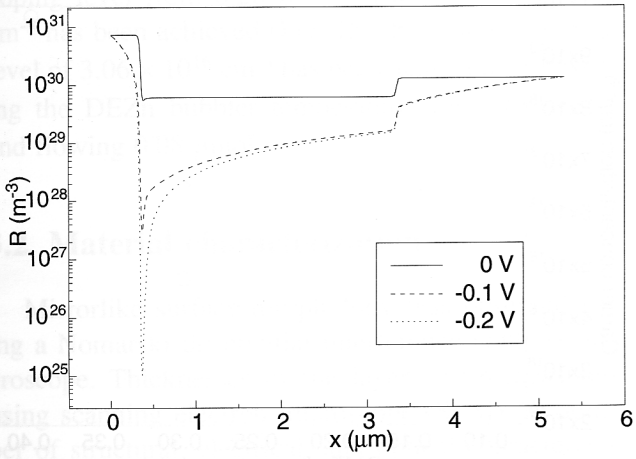


Fig. 11. Calculated profile of recombination rate at various biases.

To see the detailed behavior of the device, generation and recombination rates were also calculated.

Figures 6 to 11 show the plot of depth profile of those quantities under various reverse biases. As can be seen in the plots, the carrier extraction at a reverse bias was observed which leads to the reduced generation and recombination rates. This is expected to result in an increased responsivity under reverse bias.

## 3. Materials growth and characterization

### 3.1. MOCVD growth

MOCVD is a non-equilibrium growth technique that uses metal alkyls and hydrides as source materials in a cold walled reactor. It has established itself as a unique and important epitaxial growth technique for the stable and metastable semiconductors. In addition, MOCVD is attractive due to its ability to grow uniform layers of low background doping density and sharp interfaces, and for mass production.

For the growth of InAsSb layers, semi-insulating GaAs substrates oriented 2° off (001) towards (110) were used. The growth was carried out at a pressure of 76 torr and radio frequency induced heating was used. During the pregrowth heating, arsine overpressure was maintained in order to prevent any surface degradation. Trimethylindium (TMIn), trimethylantimony (TMSb), and 5% arsine diluted in hydrogen were used as precursors. N- and p-type doping were achieved with Sn and Zn using tetraethyltin (TESn) and diethylzinc (DEZn) as respective precursors. The growth temperature was kept at 470°C, the optimized V/III ratio was ≈ 13, and the growth rate was ≈ 0.9 μm/hr.

#### 3.1.1. Composition control

To obtain the accurate control of composition, the dependence of Sb composition of $InAs_{1-x}Sb_x$ films on various growth parameters have been studied. First, the composition dependence on the V/III ratio has been studied by keeping the TMSb and $AsH_3$ flow constant and varying the flow of TMIn. The corresponding V/III ratio varied from 15.93 to 10.62. As V/III ratio was increased, the composition of Sb in the layer was decreased from 0.80 to 0.63. Growth temperature was also varied to investigate the composition dependence on the growth temperature. When the temperature has been increased, the Sb composition

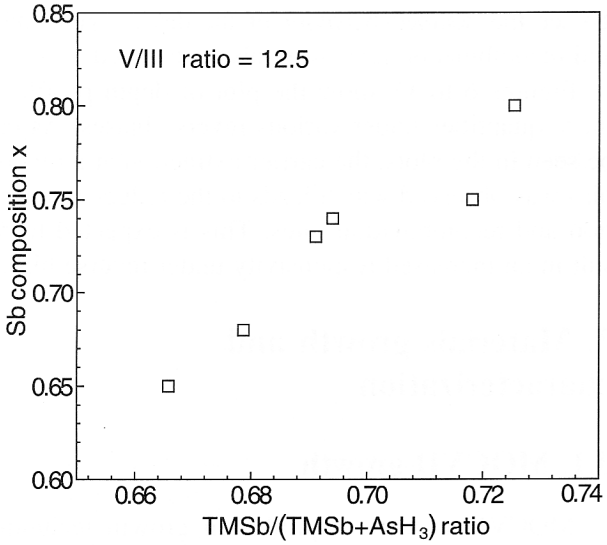


Fig. 12. Dependence of Sb composition on the group V fraction of TMSb in the vapor.

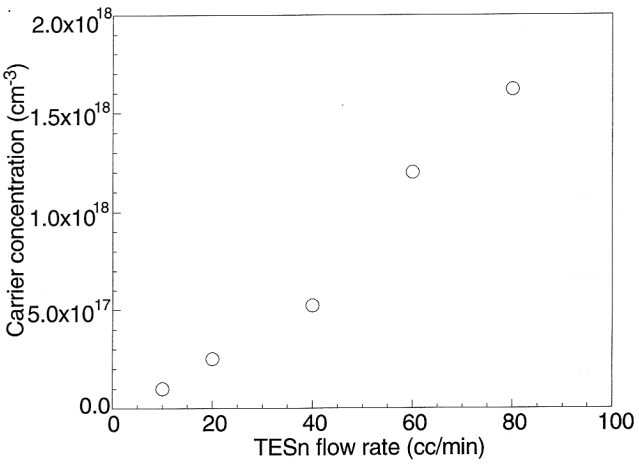


Fig. 13. N–type doping concentration dependence on TESn flow rate.

was decreased. This might be explained from the fact that $AsH_3$ decomposition has been increased as the temperature increased. As will be discussed later, the Sb composition also depends on the mole fraction of TMSb among the TMSb and $AsH_3$. If the pyrolysis of $AsH_3$ has been increased more than that of TMSb in the temperature window we tried, this would have caused the same effect as the increase of $AsH_3$ flow at the same temperature.

Most importantly, the study on the dependence of Sb composition on the group V input partial pressure ratio has been performed. The growth temperature was set at 465°C and V/III ration was 12.5. As shown in Fig. 12, group V input partial pressure ratio TMSb/(TMSb+$AsH_3$) has been varied from 0.67 to 0.73 and it resulted in the Sb composition from 0.65 to 0.80. The linear dependence of Sb composition on the partial pressure ratio was consistent with the results obtained by Biefeld et al [28].

### 3.1.2. Doping level control

In developing the devices such as photovoltaic detectors and lasers, doping of the material is a required process. Precise control of doping level is especially important for the devices operating at near ambient temperatures. Thus investigation of systematic n- and p- type doping on InSb and InAsSb has been performed. The net doping concentration was determined using Hall measurements at 77 K.

In many III-V compounds, Si is widely used n-type dopant. It has been previously used for n-type doping of InSb in MBE growth [29]. In our investigation, silane and di-silane have been tentatively used as the source for Si because of their high purity that makes them attractive for device applications. However, from Hall measurements, no significant doping was detected. This was initially attributed to the low pyrolysis efficiency of silane at our growth temperature of 465°C [30]. Furthermore, at high flow rates, surface degradation and reduced growth rates were observed. This is likely due to a parasitic reaction between the dopant source and the metalorganics in the vapor phase.

As an alternative n-type dopant source, TESn was considered. The TESn bubbler was kept at –25°C and the flow rate was varied from 0.7 nmol/min to 8.0 nmol/min, resulting in doping levels ranging from $5 \times 10^{16}$ $cm^{-3}$ to $1.6 \times 10^{18}$ $cm^{-3}$, as presented in Fig. 13. No degradation in surface morphology and X-ray FWHM were observed. Furthermore, there was no

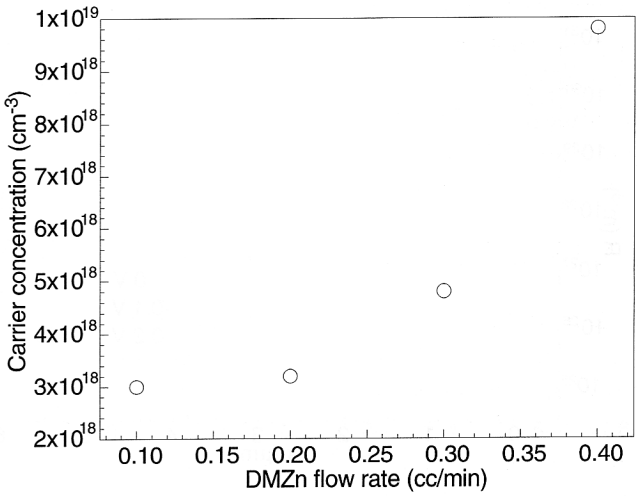


Fig. 14. P–type doping concentration as a function of DMZn flow rate.

 © 1998 COSiW SEP, Warsaw

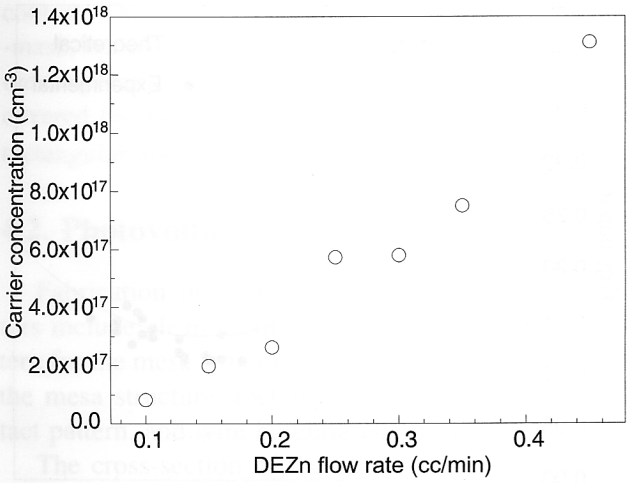


Fig. 15. P–type doping concentration as a function of DEZn flow rate.

noticeable memory effect associated with TESn, consistent with other reports [31].

P-type doping was first carried out using dimethylzinc (DMZn). Its bubbler was maintained at a constant temperature at –25°C. Zinc flow was diluted after passing through the bubbler. However, only concentrations greater than $3 \times 10^{18}$ cm$^{-3}$ was obtained even with very low capacity mass flow controller (Fig. 14).

In order to further extend our doping ranges to lower levels, diethylzinc (DEZn) has been used to replace DMZn. DEZn has a much lower vapor pressure than DMZn and is the preferred zinc source for p-type doping of III-V epitaxial alloys. The DEZn bubbler has been kept at 10°C and the flow was varied from 0.04 μmol/min to 0.2 μmol/min. The corresponding doping level from $8.26 \times 10^{16}$ cm$^{-3}$ to $1.31 \times 10^{18}$ cm$^{-3}$ has been achieved (Fig. 15). Even lower doping level of $3.06 \times 10^{16}$ cm$^{-3}$ has been achieved by lowering the DEZn bubbler temperature down to –15°C and flowing 0.08 μmol/min.

## 3.2. Material characterization

Mirrorlike surface morphology was observed using a Nomarski differential interference contrast microscope. Thicknesses of the layers were measured using scanning electron microscope (SEM). A number of structural, electrical, and optical characterizations of the epitaxial layers were performed using high resolution x-ray diffraction, Hall measurements, and optical transmission/absorption measurements.

### 3.2.1. Structural characterization

The structural characterization provides in-depth information about the crystal structure. The x-ray diffraction curve peak angular position of any crystal can be used to evaluate its lattice constant using a Bragg's law. High-resolution x-ray diffraction at (400) orientation was performed to assess the structural characteristics of the grown samples. Figure 16 shows two clearly resolved peaks for InSb and InAsSb layers with low FWHM (~300 arcsec for InAsSb) indicating the high quality of the material. Combining x-ray diffraction measurements with Vegard's law concerning the linear variation of the solid solution composition with lattice constant, the composition of ternary alloys has been determined.

### 3.2.2. Electrical characterizations

The Hall measurement is the most common characterization method used to study the electrical properties such as carrier mobility and impurity concentration. Hall data also provides information on the electrically active impurities in a semiconductor. Our Hall measurements were performed on clover-patterned samples with In contacts using Van der Pauw method at both 300 and 77 K. The current and magnetic field directions were separately reversed to eliminate the Hall-probe misalignment. For the p-doped InAsSb samples, Hall data exhibited p-type conduction with hole concentration of ~(3-10) $\times 10^{16}$ cm$^{-3}$ and hole mobility of ~ 1000 cm$^2$/Vs at 77 K. However, it

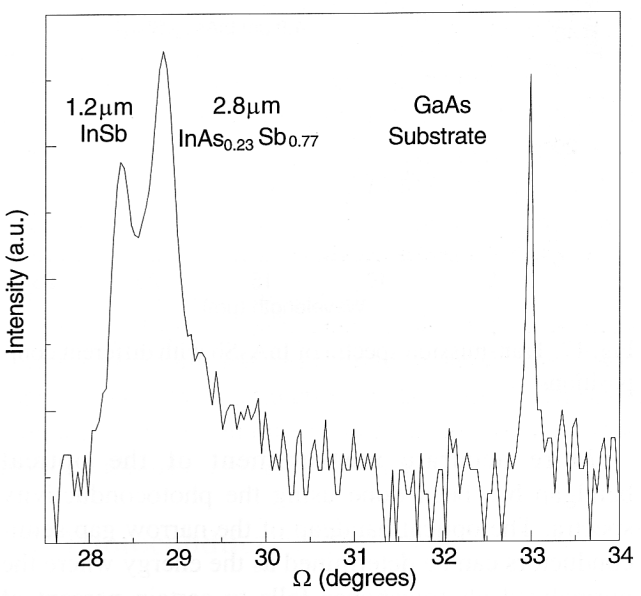


Fig. 16. X–ray diffraction spectra of InAsSb/InSb layer grown on GaAs substrates.

showed n-type conduction with electron concentration of ~3 × $10^{16}$ $cm^{-3}$ and electron mobility of ~36000 $cm^2$/Vs at 300 K. The change in sign of Hall coefficient shows that the layer is p-type and has bulk like carrier transport property [13].

### 3.2.3. Optical characterizations

Infrared transmission measurements were performed using a Fourier transform infrared (FTIR) spectrometer (Mattson, Galaxy 3000) at 300 K. The optical bandgap of the InAsSb layers can be determined using the transmission spectra to calculate the absorption coefficient of the layer. Usual definition of the optical bandgap for the narrow gap semiconductors is the photon energy for which absorption coefficient is equal to 500 $cm^{-1}$. Figure 17 shows the transmission spectra of InAsSb layers with different compositions and thicknesses at 300 K. Bandgap variation by changing the As composition can clearly be observed. Bandgap of 103 meV was derived for $InAs_{1-x}Sb_x$ layer with x = 0.77 and even narrower bandgap of 83 meV has been obtained for x = 0.65.

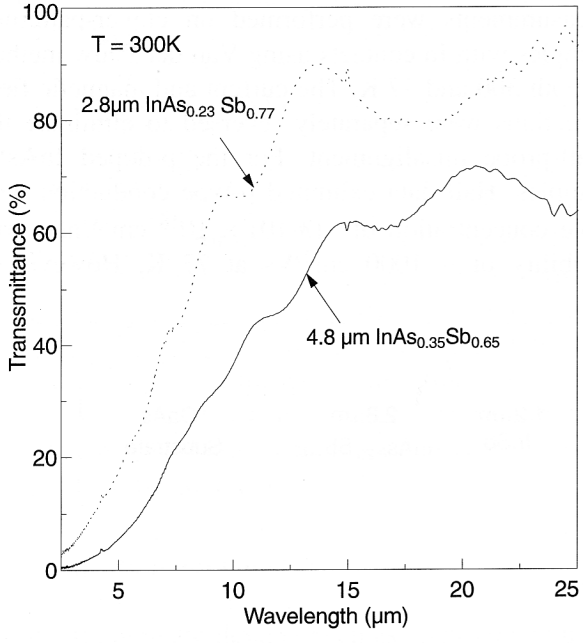


Fig. 17. Transmission spectra of InAsSb with different compositions.

More accurate measurement of the optical bandgap has been done using the photoconductivity spectra. The optical bandgap of the narrow gap semiconductors can be determined as the energy where the normalized photoresponse falls to certain percent of the maximum value. We used the 20% point in the photoresponse spectra to assess the bandgap. Figure 18 shows both theoretical and experimental 77 K bandgap of the InAsSb layers at various compositions. The experimental values are found to be lower than the theoretical values and this is attributed to the long range ordering [32,33].

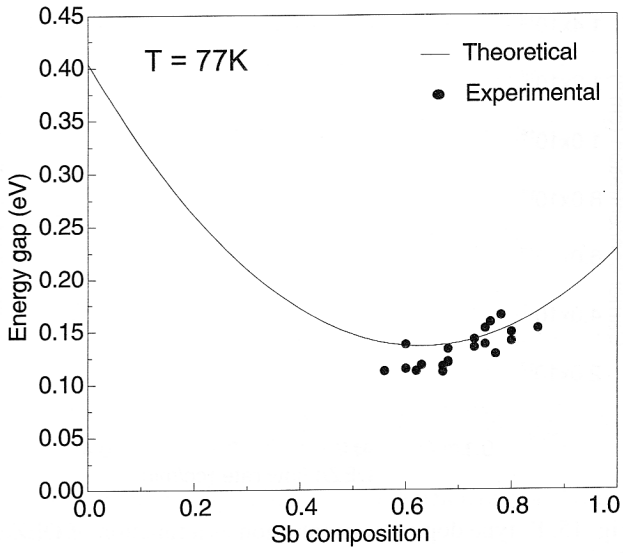


Fig. 18. Comparison of experimental and theoretical optical bandgaps for $InAs_{1-x}Sb_x$ at different compositions.

## 4. Device processing

### 4.1. Photoconductive detectors

The processing step of photoconductive detectors is quite simple. The cross-section of a photoconductive detector is schematically shown in Fig. 19. As grown wafers were cleaned using boiling solvents: TCE/TCA, acetone, and methanol/propanol. 500 Å-Ti and 3000 Å-Au are evaporated by an electron-beam-evaporator. Ti exhibits good adhesion with semiconductor surface and has good stability. Au and its alloys are commonly used to make contacts in combination with Ti in narrow-gap semiconductors. Moreover, it was easy to make Au-wire to be bonded to Au

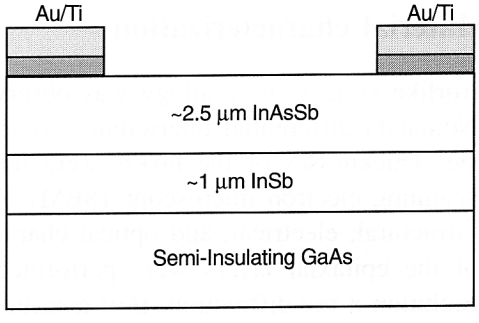


Fig. 19. Schematic of an InAsSb photoconductive detector.


© 1998 COSiW SEP, Warsaw

contact. The contact pattern is made using a metal-mask, which covers some parts of the surface during the evaporation. The resulting active area which is not covered by metallization after e-beam evaporation is rectangular and has the dimension of $3 \times 4$ mm$^2$.

## 4.2. Photovoltaic detectors

Fabrication process steps for photovoltaic detectors include cleaning of wafer, photolithography pattern for the mesa structure and the contacts, etching of the mesa structure, metalization, etching of the contact pattern, and wire bonding and package.

The cross-section of the photovoltaic detectors is schematically shown in Fig. 20. The size of the active layer is $400 \times 400$ m$^2$. The contacts are made on the $p^+$ top and $n^+$ bottom layers of the mesa structure. The structure is designed for the operation of backside (GaAs substrate side) illumination.

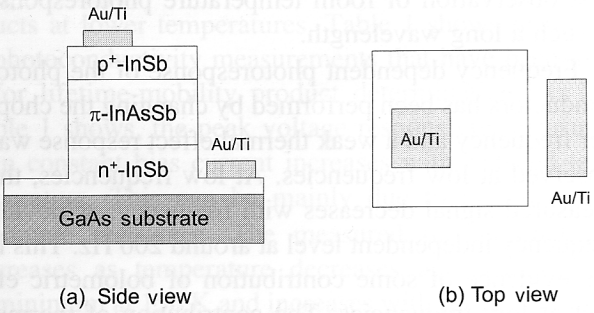


Fig. 20. Schematic of an InAsSb photovoltaic detector structure.

Before the wafer was processed, the cleaning process was done using boiling solvents: TCE/TCA, acetone, and methanol/propanol. Photolithography technique was used to make the pattern of mesa structure for chemical etching. The mesa structure was defined by wet chemical etching at room temperature. The chemical etching solution was a mixture of lactic and nitric acids.

The next step was to make the metallization and contact pattern. For the same reason discussed in the previous section, Ti and Au were used to make contacts for InAsSb devices. The contact pattern was again made using the photolithography technique and wet chemical etching. The etching solution for Au is $KI_2$:$I_2$:$H_2O$ mixture. The Ti-etching solution (HF:$H_2O$ mixture) is also selective and does not etch InAsSb or other III-V semiconductor materials.

Figure 21 shows the top view of the fabricated detector arrays. The photodetector chips were mounted on a heat sink made from copper and Au-ball bonding was made to the contacts. Since InAsSb is mechanically soft material, special care has been taken in the wire bonding process.

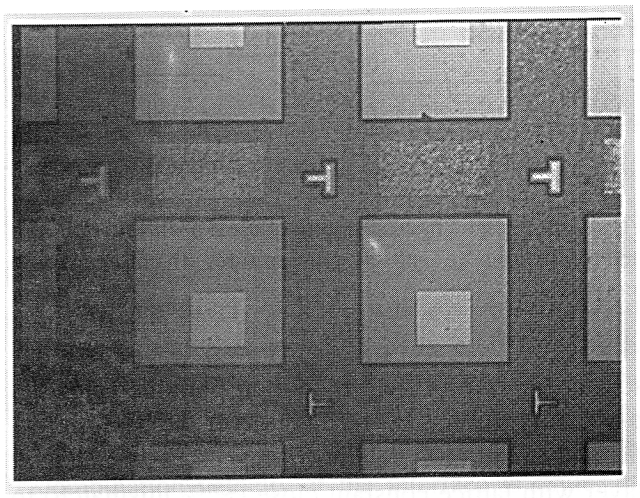

Fig. 21. Picture of the InAsSb photodetector arrays viewed from the top.

# 5. Device characterization

## 5.1. Device characterization methods

The spectral response of the InAsSb photoconductors has been measured using FTIR spectrometer. The incident radiation was usually from the front-side (InAsSb side). The spectral response of the detector has been measured at temperatures ranging from 77 to 300 K. The measured responsivity was adjusted for the frequency response of the spectrometer's internal pyroelectric detector.

In order to measure the absolute responsivity of the photodetectors, blackbody measurement setup consisting of a blackbody (Mikron-M305), a chopper (Stanford Research System-SR540), and a lock-in amplifier (EG & G-5209) has been used. The mechanical chopper operating at 400 Hz was placed between the blackbody and the detector to eliminate any bolometric effect from thermal heating. The signal was directly connected to lock-in amplifier to obtain the photovoltage. Once the photovoltage $V_p$ was measured, calculation has been done to obtain the absolute responsivity as a function of wavelength. The calculation used normalized spectral responsivity together with measured photovoltage $V_p$.

## 5.2. Photoconductive detectors

P-InAsSb/p-InSb/GaAs heterostructure has been chosen for photoconductivity studies for a number of reasons. InAsSb has been selected as the ab-

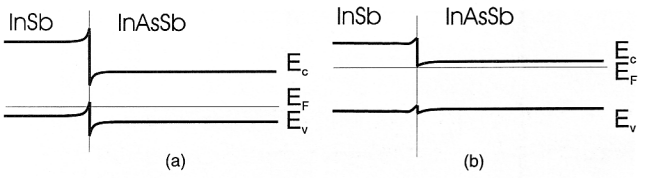


Fig. 22. Schematic band structure of ideal p–InSb/p–InAsSb heterojunctions: (a) at low temperatures, (b) at near room temperatures.

sorber material of heterojunction photodetector, its p-doping level has been selected for the best performance at 200-300 K. InSb was used as a buffer layer with lattice constant close (≈2% mismatch) to that of InAsSb with compositions optimized for operation in the 8-14 μm range. Another supposed role of InSb was confinement for electrons in the absorber layer to prevent recombination of minority carriers at absorber-substrate interface. P-type doping of InSb layer should reduce its shunting effect. GaAs is a common, high-quality, and low-cost substrate that is perfectly transparent in a wide spectral range. This makes it possible to use backside illumination both for the research purposes and to improve performance in practical applications. Schematic band diagrams of double layer heterostructures at low and high temperature are illustrated in Fig. 22.

Figure 23 shows the spectral responsivities of the photoconductor sample at 200 K and 300 K [34]. The peak responsivity at 300 K is about $4.0 \times 10^{-3}$ V/W at 8 μm under a bias voltage of 1 volt. A cut-off wavelength around 14 μm was observed at 300 K despite the doping of the layer not being optimized for room

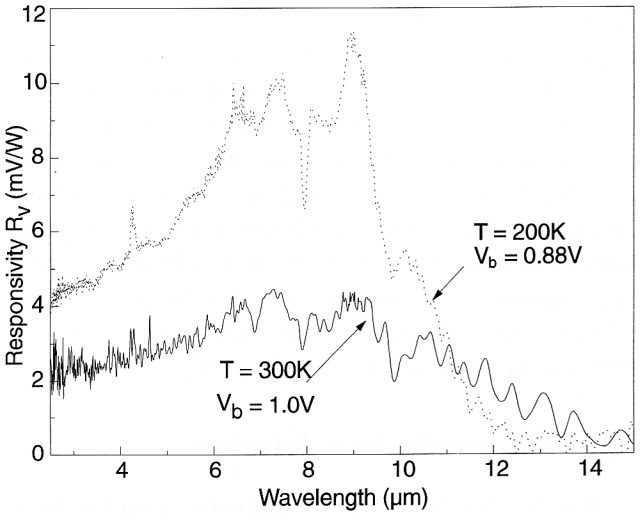


Fig. 23. Spectral response of an $InAs_{0.23}Sb_{0.77}$ photoconductor at 200 K and 300 K.

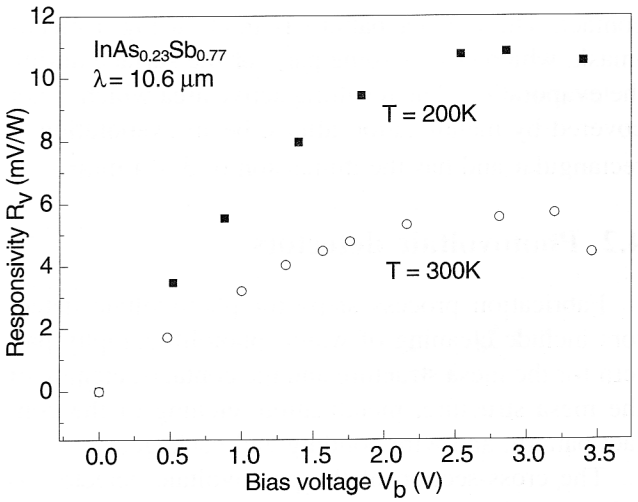


Fig. 24. Voltage-dependent responsivity of an $InAs_{0.23}Sb_{0.77}$ photoconductor at 10.6 μm.

temperature operation. These measurements were the first observation of room temperature photoresponse at such a long wavelength.

Frequency dependent photoresponse of the photoconductors has been performed by changing the chopper frequency and a weak thermal effect response was observed at low frequencies. At low frequencies, the measured signal decreases with frequency; achieving frequency independent level at around 200 Hz. This is the evidence of some contribution of bolometric effect at low frequencies. The contribution of thermal response was negligible at frequencies used by FTIR and blackbody measurements.

To obtain the photoconductivity lifetime, bias voltage dependent responsivity at 10.6 μm has been measured (Fig. 24). The responsivity increased with applied voltage and reached saturation at around 3 volts, which corresponds to a value of $5.8 \times 10^{-3}$ V/W at 300 K and $1.08 \times 10^{-2}$ V/W at 200 K. Based on the voltage responsivity, the electron mobility-effective carrier lifetime product $\mu_e\tau$ and effective carrier lifetime $\tau$ can be derived. According to the simple theory of photoconductivity [35], the voltage responsivity is

$$R_v = \frac{q\lambda}{hc}\frac{\eta\mu_e\tau V_b R_D}{L^2}\left(1+\frac{1}{b}\right) \qquad (2)$$

where q is the electron charge, λ is the wavelength, η is the quantum efficiency, b is the electron-to-hole mobility ratio, L is the detector length, $V_b$ is the bias voltage, and $R_D$ is the detector resistance. Assuming an internal quantum efficiency of 1, the quantum efficiency η has been calculated using

 © 1998 COSiW SEP, Warsaw

$$\eta = (1-r)\frac{(1-e^{-\alpha t})}{(1-re^{-\alpha t})} \quad (3)$$

where r is the reflectance, α is the absorption coefficient, and t is the thickness of the layer. The $\mu_e\tau$ product has been determined using Eq. (2). If $\mu_e$ is known, τ can be estimated. Using the electron mobility at 300 K, where intrinsic electrons dominate the Hall measurements, the effective lifetime was estimated to be 0.14 ns. The photoconductive lifetime at 300 K (≈0.14 ns) is close to the theoretical limit set by Auger recombination in InAsSb with bandgap of 0.103 eV. The agreement is quite good taking into account factors of a great uncertainty involved in the theoretical calculations. The estimated Johnson noise limit of detectivity of the photoconductor at room temperature is $\approx 3.27 \times 10^7$ cmHz$^{1/2}$/W.

Absolute measurements of photoconductivity response were used for the determination of $\mu_e\tau$ products at lower temperatures. Table 1 shows results of photoconductivity measurements that have been used for lifetime-mobility product determination. As Table 1 shows, the peak voltage responsivity measured in constant bias current increases with reduced temperature. This can be mainly due to the increased sample resistance. The measured $\mu_e\tau$ product decreases as temperature decreases and achieves its minimum at 150 K and increases with further cooling.

Table 1. Results of photoconductivity measurements

| T (K) | $V_b$ (V) | $R_D$ (Ω) | V (μV) | $R_v^{BB}$ (V/W) | $R_{vp}$ (V/W) | $\mu_e\tau$ (cm$^2$/V) |
|---|---|---|---|---|---|---|
| 77 | 3.4 | 469 | 35.2 | $2.24 \times 10^{-1}$ | $4.65 \times 10^{-1}$ | $1.48 \times 10^{-5}$ |
| 150 | 3.6 | 557 | 12.4 | $7.88 \times 10^{-2}$ | $1.28 \times 10^{-1}$ | $3.62 \times 10^{-6}$ |
| 200 | 2.6 | 334 | 18.0 | $1.14 \times 10^{-1}$ | $1.81 \times 10^{-1}$ | $8.22 \times 10^{-6}$ |
| 250 | 0.78 | 54.3 | 2.05 | $1.3 \times 10^{-2}$ | $1.95 \times 10^{-2}$ | $2.33 \times 10^{-5}$ |
| 300 | 0.28 | 18 | 0.18 | $1.14 \times 10^{-3}$ | $2.10 \times 10^{-3}$ | $2.46 \times 10^{-5}$ |

The $\mu_e\tau$ products at lower temperatures are quite lower than expected. As the low temperature electron mobility is not known, we cannot determine the effective photoconductivity lifetime at low temperatures. The possible reasons for a short lifetime-mobility product are non-fundamental recombination mechanisms, such as Shockly-Read-Hall, surface or interface recombination. The time necessary for electron to diffuse through the layer with thickness t is

$$\tau_D = \frac{t^2}{2D_e} \quad (4)$$

where $D_e$ is the electron diffusion coefficient. According to Einstein relation $D_e = kT\mu_e/q$ and

$$\tau_D\mu_e = \frac{t^2 q}{2kT} \quad (5)$$

When the layer thickness t is 2.8 μm, the calculated $\mu_e\tau_D$ value is $\approx 1.5 \times 10^{-6}$ cm$^2$/V at 150 K. Taking into account the fact that the generation-recombination of carriers occurs not only at the surface but within entire layer thickness and that the recombination velocity at the interface is finite, the calculated diffusion limited lifetime-electron mobility product is comparable to the experimental values. So we concluded that the effective lifetime at low temperatures is controlled by the recombination at the InAsSb/InSb interface.

## 5.3. Photovoltaic detectors

The photovoltaic detectors consisted of p$^+$-InSb/p-InAsSb/n$^+$-InSb double heterojunction. The grown structures were processed using photolithography, chemical etching, and metallization techniques as described earlier. The measurement set-up was identical to that for photoconductor measurement except that no bias circuit was necessary.

Figure 25 shows the voltage response at various temperatures. The temperature-dependent cut-off wavelength is clearly observed. Photoresponse up to 13 μm has been obtained at 300 K in an $InAs_{0.15}Sb_{0.85}$

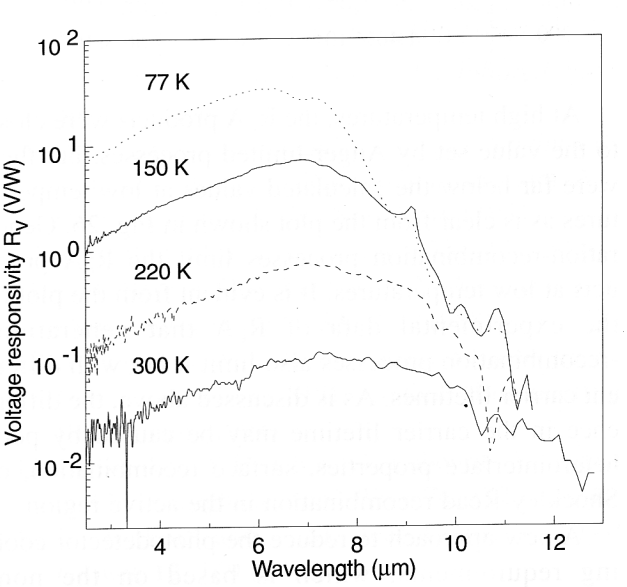


Fig. 25. Spectral response of InAsSb photovoltaic detector at various temperatures.

detector [36]. The peak voltage-responsivity is $9.13 \times 10^{-2}$ V/W at 300 K. At 77 K, it is only $2.85 \times 10^{1}$ V/W, which is much lower than the expected value. Possible reasons are the poor interface properties due to the lattice mismatch between the absorber and contact layers and high dark current due to the high dopping level in the active layer.

As the series resistance is much higher than the junction resistance at high temperatures, we could not measure the $R_oA$ product directly from the I-V curve. So the $R_oA$ product has been derived using

$$R_v A = \frac{\lambda \eta q R_o A}{hc} \qquad (6)$$

where $\lambda$ is the wavelength, $\eta$ is the quantum efficiency, q is the electron charge, h is the Planck's constant, c is the velocity of light, and $R_v$ is the voltage responsivity. Table 2 shows the responsivity-area product and resistance-area product of the $InAs_{0.15}Sb_{0.85}$ photodiode at various temperatures [37].

Table 2. Peak voltage responsivity-area product and corresponding resistance-area product of InAsSb photovoltaic detectors at various temperatures

| T (K) | $R_vA$ (Vcm$^2$/W) | $R_oA$ ($\Omega$cm$^2$) |
|---|---|---|
| 77 | $4.56 \times 10^{-2}$ | $3.15 \times 10^{-2}$ |
| 100 | $2.58 \times 10^{-2}$ | $1.53 \times 10^{-2}$ |
| 150 | $9.68 \times 10^{-3}$ | $5.73 \times 10^{-3}$ |
| 200 | $1.64 \times 10^{-3}$ | $9.71 \times 10^{-4}$ |
| 220 | $1.03 \times 10^{-3}$ | $6.10 \times 10^{-4}$ |
| 250 | $5.57 \times 10^{-4}$ | $3.30 \times 10^{-4}$ |
| 300 | $1.46 \times 10^{-4}$ | $7.56 \times 10^{-5}$ |

At high temperatures, the $R_oA$ products were close to the value set by Auger-limited processes, but they were far below the calculated values at low temperatures as is clear from the plot shown in Fig. 26. Generation-recombination processes limit the $R_oA$ products at low temperatures. It is evident from the plot of the experimental data of $R_oA$ that generation--recombination processes also limit it but with different carrier lifetimes. As is discussed above, the difference in the carrier lifetime may be caused by poor heterointerface properties, surface recombination, or Shockley-Read recombination in the active region.

A new approach to reduce the photodetector cooling requirements, which is based on the non--equilibrium mode of operation, has been proposed by British workers and applied for InSb based infrared

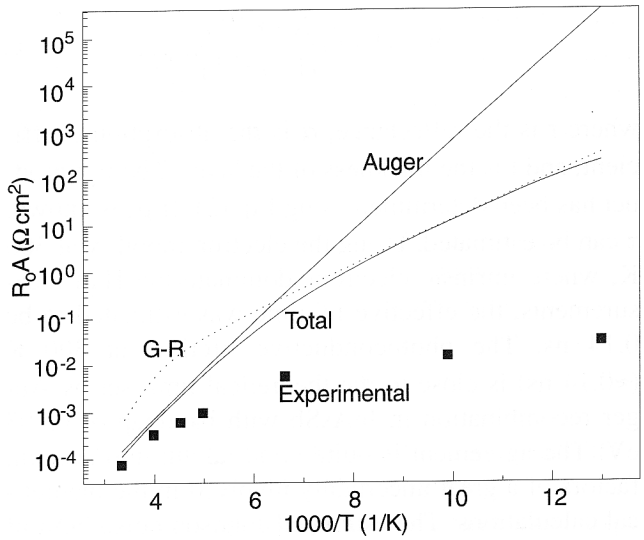


Fig. 26. Comparison of experimental $R_oA$ values with the theoretical limit.

devices [38,39]. The ultimate signal-to-noise performance of the intrinsic semiconductor photodetectors is limited by the statistical fluctuation of generation and recombination rate, which in the high temperature photodetectors is determined by the Auger processes. The noise associated with recombination can be reduced by spatial separation of generation and recombination (G-R) in a device. The depletion could be achieved in a biased lightly doped homojunction or heterojunction contact and this results in a reduced G-R rates, which was demonstrated in the numerical calculation. Reduction in G-R rates results in an increased responsivity. Preliminary experiments on the biased mode operation of the InAsSb photovoltaic de-

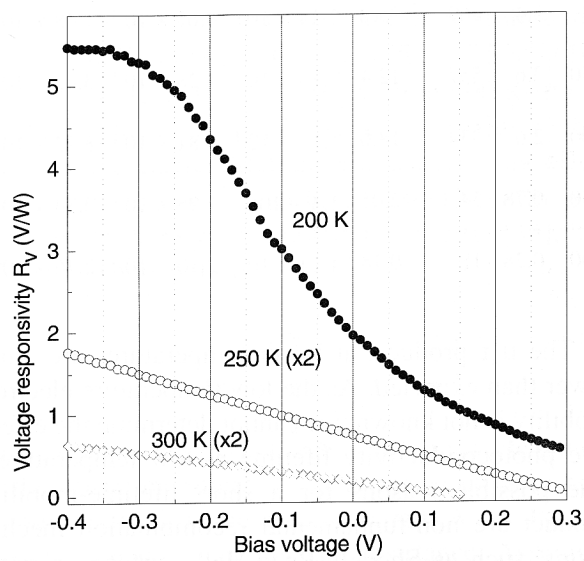


Fig. 27. Bias dependent voltage responsivity of the $InAs_{0.15}Sb_{0.85}$ photovoltaic detector.


© 1998 COSiW SEP, Warsaw

tectors have been performed. As shown in Fig. 27, the voltage responsivity at near room temperatures has been increased by a factor of ~3 at 0.4V reverse bias. Further increase in responsivity can be achieved through lower doping level.

## 6. Conclusions

In this work, MOCVD growth and material properties of InAsSb epitaxial films have been studied for the infrared detector applications. InSb was the starting point for the development of InAsSb material system. InAsSb is a particularly interesting material system for the detectors operating at near room temperatures because the cut-off wavelength can be extended enough to cover the entire 8–14 μm infrared window. Study on the development of InAsSb detectors operating at near room temperatures have been performed.

Using the highly developed growth technique, MOCVD, high quality InAsSb layers have been grown on semi-insulating GaAs substrates. The crystal quality and compositions of the grown layers have been identified through x-ray diffraction and utilizing the Vegard's law. Optical bandgaps obtained through the optical characterizations were lower than the theoretical values and showed the feasibility of the InAsSb for LWIR applications. As a step towards the realization of photodetectors, study on the doping has been performed. Both n- and p-type doping have been successfully obtained by Sn and Zn using TESn and DEZn as sources, respectively.

For the first time, photoconductive detectors based on InAsSb have been operated up to room temperature with cut-off wavelength exceeding 13 μm. The doping level of the active layer has been determined through the minimization of the Auger generation and recombination. Through the voltage dependent measurement of the responsivity, we were able to obtain the photoconductive lifetime of 0.14 ns and estimated detectivity of $3.27 \times 10^7$ cmHz$^{1/2}$/W at 300 K. Detailed analysis on the photoconductivity measurements have been performed to study more about the surface and interface related problems.

Also, InAsSb photovoltaic detectors on GaAs substrates have been fabricated and found to operate up to room temperature. The cut-off wavelength of an $InAs_{0.15}Sb_{0.85}$ photovoltaic detector was about 13 μm at 300 K. The optimized detector structures have been designed through analytical and numerical device modeling. The peak voltage-responsivity was $9.13 \times 10^{-2}$ V/W at 300 K. The derived $R_oA$ product was close to the limit set by the Auger processes at room temperature.

In spite of the large lattice mismatch between the InAsSb and GaAs, InAsSb detectors have exhibited good characteristics and showed their feasibility for the near room temperature LWIR photodetectors as an alternative to HgCdTe detectors. Preliminary results on the InAsSb detectors are encouraging, but more improvement of the detector performance is necessary for the practical applications. These improvements are expected to be achieved by employing techniques such as large bandgap heterojunction barrier layers, non-equilibrium mode operation, optical resonant cavity, and optical immersion.

## References


1. E.L. Derenniak and G.D. Boreman, *Infrared Detectors and Systems*, John Wiley & Sons, New York (1996).
2. W.L. Wolfe and G.J. Zissis, *The Infrared Handbook*, ERIM, Ann Arbor (1989).
3. A. Rogalski, *Infrared Photon Detectors*, SPIE Optical Engineering, Bellingham (1995).
4. C.T. Elliott, *Handbook of Semiconductors*, Vol. 4, edited by T.S. Moss, North Holland, Amsterdam (1981).
5. R.M. Broudy and V.J. Mazurczyk, *Semiconductors and Semimetals*, Vol. 18, edited by R.K. Willardson and A.C. Beer, Academic Press (1981).
6. N.T. Gordon, *Semicon. Sci. Technol.* **6**, C107 (1991).
7. Z. Djuric, J. Piotrowski, Z. Jaksic, and Z. Djinovic, *Electron. Lett.* **24**, 1590 (1988).
8. J. Piotrowski and T. Niedziela, *Infrared Phys.* **30**, 113 (1990).
9. P.W. Kruse, *Semiconductors and Semimetals*, Vol. 18, edited by R.K. Willardson and A.C. Beer, Academic Press, New York (1981).
10. R.M. Biefeld, *J. Cryst. Growth* **75**, 255 (1986).
11. C.G. Bethea, B.F. Levine, M.Y. Yen, and A.Y. Cho, *Appl. Phys. Let.* **53**, 291 (1988).
12. A. Rogalski, *New Ternary Alloy Systems for Infrared Detectors*, SPIE Optical Engineering, Bellingham (1994).
13. C. Besikci, Y.H. Choi, G. Labeyrie, E. Bigan, and M. Razeghi, *J. Appl. Phys.* **76**, 5820 (1994).
14. B. Joukoff and A.M. Jean-Louis, *J. Cryst. Growth* **12**, 169 (1972).
15. J.L. Zilko and G.E. Greene, *Appl. Phys. Lett.* **33**, 254 (1978).

16. A.J. Noreika, W.J. Takei, M.H. Francombe, and C.E.C. Wood, *J. Appl. Phys.* **53**, 4932 (1982).
17. K. Oe, S Ando, and K. Sugiyama, *Jpn. J. Appl. Phys.* **20**, L303 (1981).
18. T.P. Humphreys, P.K. Chiang, S.M. Bedair, and N.R. Parikh, *Appl. Phys. Lett.* **53**, 142 (1988).
19. K.T. Huang, C.T. Chiu, R.M. Cohen, and G.B. Stringfellow, *J. Appl. Phys.* **75**, 2857 (1994).
20. J.J. Lee, J.D. Kim, and M. Razeghi, *Appl. Phys. Lett.* **70**, 3266 (1997).
21. J.J. Lee, J.D. Kim, and M. Razeghi, *Appl. Phys. Lett.* **71**, 2298 (1997).
22. M. Schilfgaarde and A. Sher, *Appl. Phys. Lett.* **62**, 1857 (1993).
23. Y.H. Choi, C. Besikci, R. Sudharsanan, and M. Razeghi, *Appl. Phys. Lett.* **63**, 361 (1993).
24. J.D. Kim, E. Michel, S.J. Park, J. Xu, S. Javadpour, and M. Razeghi, *Appl. Phys. Lett.* **69**, 343 (1996).
25. A. Rogalski, *Prog. Quant. Electr.* **13**, 191 (1989).
26. A. Rogalski, R. Ciupa and W. Larkowski, *Solid-State Electr.* **39**, 1593 (1996).
27. M. Kurata, *Numerical Analysis of Semiconductor Devices*, Lexington Books, Toronto (1982).
28. R.M. Biefeld, *J. Cryst. Growth* **77**, 392 (1986).
29. S.D. Parker, R.L. Williams, R. Droopad, R.A. Stradling, K.W.J. Barnham, S.N. Holmes, J. Laverty, C.C. Phillips, E. Skuras, R. Thomas, X. Zhang, A. Staton-Bevan, and D.W. Pashley, *Semicon. Sci. Technol.* **4**, 663 (1989).
30. E. Veuhoff, T.F. Kuech, B.S. Meyerson, *J. Electrochem. Soc.* **132**, 1958 (1985).
31. R.M. Biefeld, J.R. Wendt, and S.R. Kurtz, *J. Crystal Growth* **107**, 836 (1991).
32. R.A. Stradling, *Semicond. Sci. Technol.* **6**, C52 (1991).
33. S.R. Kurtz, L.D. Dawson, R.M. Biefeld, D.M. Follstaedt, and B. L. Doyle, *Phys. Rev.* **B 46,** 1909 (1992).
34. J.D. Kim, D. Wu, J. Wojkowski, J. Piotrowski, J. Xu, and M. Razeghi, *Appl. Phys. Lett.* **68**, 99 (1996).
35. S.M. Sze, *Physics of Semiconductor Devices*, Wiley, New York (1981).
36. J.D. Kim, S. Kim, D. Wu, J. Wojkowski, J. Xu, J. Piotrowski, E. Bigan, and M. Razeghi, *Appl. Phys. Lett.* **67**, 2645 (1995).
37. E. Michel, J. D. Kim, S. Park, J. Xu, I. Ferguson, and M. Razeghi, *Proc. SPIE* **2685**, 105 (1996).
38. T. Ashley, C.T. Elliott, and A. T. Harker, *Infrared Phys.* **26**, 303 (1986).
39. T. Ashley, A.B. Dean, C.T. Elliott, M.R. Houlton, C.F. McConville, H.A. Tarry and C.R. Whitehouse, *Proc. SPIE* **1361**, 238 (1990).

 © 1998 COSiW SEP, Warsaw